Energy 239 (2022) 121876

Contents lists available at ScienceDirect

Energy

journal homepage: www.elsevier.com/locate/energy

A control-oriented large eddy simulation of wind turbine wake considering effects of Coriolis force and time-varying wind conditions

Guo-Wei Qian, Yun-Peng Song, Takeshi Ishihara*

Department of Civil Engineering, School of Engineering, The University of Tokyo, 7-3-1 Hongo, Bunkyo-ku, Tokyo, 113-8656, Japan

ARTICLE INFO

Article history:
Received 10 June 2021
Received in revised form
2 August 2021
Accepted 21 August 2021
Available online 26 August 2021

Keywords:
Large eddy simulation
Actuator line model
Wind turbine wake
Wind turbine control
Coriolis force
Time-varying wind condition

ABSTRACT

A control-oriented large eddy simulation (LES) code is developed to predict wind turbine wake and is validated by laboratory-scale and utility-scale wind turbines. Firstly, the wind turbine control algorithms including torque, pitch and yaw controls are implemented in LES with Actuator Line Model (ALM). Two sets of numerical simulations under uniform inflow with time-varying wind speeds and wind directions are performed. The simulated thrust and torque forces agree well with those calculated by the aeroelastic code, FAST. The predicted mean velocity and turbulence intensity in the wake of a laboratory-scale wind turbine show favorable agreement with those measured in wind tunnel experiments. The blade rotation induced dynamic effects on wake flows and rotor loading are well reproduced by ALM. Finally, numerical simulations for a utility-scale wind turbine are conducted, in which the ambient flow filed with time-varying wind speeds and wind directions are generated based on the wind condition measured by the Met-mast and the Coriolis force effect is incorporated as well. The predicted time series of control signals and power production agree well with the wind turbine SCADA data and the predicted mean wind speed in the wake region show favorable agreement with those measured by Doppler scanning LiDAR.

1. Introduction

The potential of wind farm control by coordinating the greedy pitch or yaw control operations across the wind turbines has been studied more than a decade, the main objectives of which include increasing power production, reducing turbine loads, and providing electricity grid support services [1]. However, due to the high cost and safety issues in the field test, the lack of validation is one of the main barriers to wind farm control on an industrial scale [2]. Therefore, an efficient and accurate numerical approach to simulate the turbine controls and wake flows is of urgent need in order to evaluate the wind farm control more comprehensively before the engineering implementation. Such numerical frameworks are normally referred to as wind farm simulators. To this day, a number of wind farm simulators have been developed, and a review of state-of-the art LES codes for high fidelity wind farm simulations can be found in Ref. [3]. In summary, there are mainly the following aspects associated with LES codes for wind farm simulation: rotor model, wind turbine control, aeroelasticity, atmospheric boundary layer, including micro-scale ambient turbulence, meso-scale time-variation in mean wind speed and wind direction (geophysical effects), Coriolis force, terrain and forest.

Regarding rotor model, three strategies have been developed and used in wind farm simulations: Actuator Disk Model without and with rotation (ADM-NR, ADM-R), Actuator Line Model (ALM), and Actuator Surface Model (ASM). Compared with ALM and ASM, the ADM model is preferred in wind farm simulations due to its simplicity of implementation and relative low computational cost. The ability of ADM-R to accurately estimate time-averaged wake characteristics and power productions of utility-scale wind farms has been demonstrated by Wu and Porté-Agel [4]. However, the main limitation of the ADM is that it is unable to capture blade tip and root vortices. To overcome this limitation, ALM was developed by Sørensen and Shen [5], which allows for detailed study of rotor and wake dynamics. ALM has been employed in many recent large eddy simulations for wind turbines and wind farms [6,7] and shown to be capable of simulating with a moderately computational cost in comparison to a full rotor modelling. However, a systematic comparison between ADM and ALM, including both statistical and time-dependent variables regarding wake flows and dynamic loadings have not yet been performed.

A wind turbine controller was also implemented in existing LES

* Corresponding author.
E-mail addresses: qian@bridge.t.u-tokyo.ac.jp (G.-W. Qian), ishihara@bridge.t.u-tokyo.ac.jp (T. Ishihara).

https://doi.org/10.1016/j.energy.2021.121876
0360-5442/

framework to allow for active control on a turbine level and further plant level. Deskos et al. [6] only incorporated the torque control in the below-rated region, where the turbine adapts the rotor speed according to the prevailing wind speed. In addition to torque control, Guggeri and Draper [7] added the pitch control as well to enable a regulation of generator speed in the above-rated region. The yaw control, making the rotor axis of a wind turbine aligned with dominating wind direction, also plays an important role in maximizing energy extraction from the wind. Moreover, due to uncertainty of wind direction, turbines often experience unintentional yaw misalignment, which can significantly induce a power loss [8,9] and affect the wake behaviors and fatigue loads [10], thus it should be carefully modelled in the wake steering control as well [11]. However, the yaw control strategy under time varying wind directions has not been implemented and investigated in the above mentioned LES codes.

Wind turbine wake and power production depend significantly on inflow wind conditions. Most large eddy simulations of wind farm use a turbulent inflow condition with a constant mean wind speed and wind direction. However, it differs from realistic wind conditions due to the absence of meso-scale time-variation in wind speed and direction. To simulate the effects of time-varying wind direction in LES for a wind farm, Munters et al. [12] proposed a concurrent precursor method in which the periodic precursor domain is horizontally rotating flowing the varying wind direction. More recently, Stieren et al. [13] proposed a more straightforward method by treating the simulation domain as a non-inertial rotating reference frame with corresponding Coriolis force and centrifugal forces, which has the benefits of avoiding a sequence of geometric interpolations associated in rotating simulation domain. Both studies have revealed that time-varying wind direction influence the wind farm power production. However, the wind turbine control is not included in their simulation, which can significantly affect the wind field and power production in wind farms.

When modelling the wind turbine or wind farm in real scale, another issue should be considered is the earth rotation induced Coriolis force. As discussed by van der Laan and Sørensen [14], the Coriolis force in the northern hemisphere deflects a wind turbine wake to the right with respect to the incoming wind. This will significantly affect the wake steering control strategies. As recently investigated by Nouri et al. [15]; for columns aligned with the wind direction, positive yaw offset can lead to an overall increase in the power production due to the Coriolis force effect, while negative yaw offset reduces it. However, the modelling of Coriolis force effects on wind turbine wakes are lack of validations by the field measurements in the previous research. Therefore, it is necessary to comprehensively implement torque, pitch and yaw controllers and incorporate the Coriolis force in the LES codes, and then validate the numerical results by the field measurements of utility-scale wind turbines.

In this study, the numerical model, including governing equation, actuator line model, and wind turbine control algorithm are presented in Section 2. Two sets of benchmark wind conditions with time-varying wind speed and wind direction are utilized to verify the behavior of developed wind turbine controller in Section 3. The wake flow of the laboratory-scale wind turbine is then predicted by using ALM and compared with those obtained from the wind tunnel experiment in section 4. Finally, the developed control-oriented large eddy simulation considering time-varying wind condition and Coriolis force is applied to a utility-scale 2.4 MW wind turbine, where the predicted turbine operation conditions and wakes are compared with those obtained from field measurement in Section 5. The conclusions of this study are summarized in Section 6.

2. Numerical model

The governing equation of LES is firstly introduced in Section 2.1. The ALM used to parameterize the rotor aerodynamics is described in Section 2.2. The wind turbine control algorithms for torque, pitch and yaw are then explained in Section 2.3. Finally, the wind turbine configuration regarding the geometry, steady state thrust curve and power curve are presented in Section 2.4.

2.1. Governing equation

The finite volume method (FVM) is applied for the discretization of the governing partial differential equations. In LES, the incompressible Navier-Stokes equations are filtered as follows:

$$\frac{\partial \rho \tilde{u}_i}{\partial x_i} = 0 \tag{1}$$

$$\frac{\partial}{\partial t}(\rho \tilde{u}_i) + \frac{\partial}{\partial x_j}(\rho \tilde{u}_i \tilde{u}_j) = \frac{\partial}{\partial x_j}\left(\mu \frac{\partial \tilde{u}_i}{\partial x_j}\right) - \frac{\partial \tilde{p}}{\partial x_i} - \frac{\partial \tau_{ij}}{\partial x_j} + f_{rot,i} + f_{wd,i} + f_{cor,i} \tag{2}$$

where $\tilde{u}_i$ (i=1, 2 and 3) denote the velocity component in ith direction, $\tilde{p}$ is the pressure, ρ is the air density, and μ is the dynamic viscosity. The momentum source term $f_{rot,i}$ represents the rotor induced aerodynamic force which will be discussed in Sections 2.2. $f_{wd,i}$ is the external force associated with time-varying wind direction in a non-inertial rotating reference frame [13], which is expressed as

$$f_{wd,i} = -2\rho\omega\tilde{u}_j\varepsilon_{ij3} + \rho\omega^2 x_i(\delta_{i1} + \delta_{i2}) \tag{3}$$

where ω is half the rate of wind direction ϑ change in time as follows:

$$\omega = 0.5\frac{\partial \vartheta}{\partial t} \tag{4}$$

$f_{cor,i}$ denotes the Coriolis force induced by earth rotation. Taken that x_3 is up (at the location on the earth), then the Coriolis force is calculated by the following equations

$$f_{cor,i} = -2\rho\varepsilon_{ijk}\Omega_j\tilde{u}_k \tag{5}$$

$$\Omega_j = \omega_e \begin{bmatrix} 0 \\ \cos\phi \\ \sin\phi \end{bmatrix} \tag{6}$$

where ε_{ijk} is the alternating unit tensor. Ω_j is the rotation rater vector at the location on the earth surface, ω_e is the earth rotation rate ($\sim 2.95 \times 10^{-5}$ rad/s), and ϕ is the latitude.

Smagorinsky-Lill model [16] is used to calculate the subgrid-scale (SGS) Reynolds stress τ_{ij} as follows.

$$\tau_{ij} = -2\mu_t \tilde{S}_{ij} + \frac{1}{3}\tau_{kk}\delta_{ij} \tag{7}$$

where $\tilde{S}_{ij}$ is the rate-of-strain tensor defined as follows:

$$\tilde{S}_{ij} \equiv \frac{1}{2}\left(\frac{\partial \tilde{u}_i}{\partial x_j} + \frac{\partial \tilde{u}_j}{\partial x_i}\right) \tag{8}$$

δ_{ij} is the Kronecker delta and the term $(\delta_{ij}/3)\cdot\tau_{kk}$ is absorbed into the pressure term following standard practice [17]. μ_t denotes the eddy viscosity, which is modelled as:

$$\mu_t = \rho L_S^2 |\tilde{S}| = \rho L_S^2 \sqrt{2\tilde{S}_{ij}\tilde{S}_{ij}} \tag{9}$$

where L_S denotes the mixing length for subgrid-scales and it is calculated by:

$$L_S = min\left(\kappa\delta, C_S V^{1/3}\right) \tag{10}$$

κ is the von Karman constant, 0.42, δ is the distance to the closet wall and V is the volume of a computational cell. C_S is Smagorinsky constant and is determined as 0.032 [18].

2.2. Actuator line model

The effect of the rotor induced forces on the flow is parameterized by using the Actuator Line Model [5] . In this model, the turbine blades are represented by three rotating lines which are discretized into several nodes, where the lift and drag forces are calculated based on the blade element theory [19]. Fig. 1a shows the schematic of ALM model, where x is streamwise direction aligned with the incoming wind speed U_0. The relation between wind velocity and forces acting on a blade element of length dr located at the radius r is shown in Fig. 1b, where n and t denote the axial and tangential directions respectively, α is the angle of attack, β is the local pitch angle and ψ is the angle between the relative velocity and the rotor plane. dF_L and dF_D are the lift and drag forces acting on the blade element and given by:

$$dF_L = \frac{1}{2}\rho W^2 c C_L dr,\ dF_D = \frac{1}{2}\rho W^2 c C_D dr \tag{11}$$

where c is the chord length, C_L and C_D are the lift and drag coefficients, respectively. W is the local relative velocity with respect to the blade element and is defined as:

$$W = \sqrt{U_n^2 + (\Omega r - U_t)^2} \tag{12}$$

Where U_n and U_t are the axial and tangential velocities of the incident flow at the local blade element position, and Ω is the rotor speed. The resulting axial force dF_n and tangential force dF_t on the blade element can be expressed as:

$$dF_n = dF_L cos\psi + dF_D sin\psi \tag{13}$$

$$dF_t = dF_L sin\psi - dF_D cos\psi \tag{14}$$

Consequently, the aerodynamic force per spanwise unit length $\boldsymbol{f}$ in the global coordinate system of computational domain is calculated as follows

$$\boldsymbol{f} = \frac{d\boldsymbol{F}}{dr} = \begin{bmatrix} cos\,\gamma & sin\,\gamma\,cos\,\Phi \\ sin\,\gamma & -cos\,\gamma\,cos\,\Phi \\ 0 & -sin\,\Phi \end{bmatrix} \begin{bmatrix} \frac{dF_n}{dr} \\ \\ \frac{dF_t}{dr} \end{bmatrix} \tag{15}$$

where, γ is the yaw offset angle of turbine respect to the incoming wind direction, Φ denotes the azimuth angle of blade position. A 3D Gaussian distribution function is applied to project the above aerodynamic force smoothly from actuator-line nodes to computational cells in the CFD simulation by the following equations.

$$\boldsymbol{f}_{\mathbf{rot}} = \sum_{b=1}^{B}\sum_{n=1}^{N} \boldsymbol{f}_{b,n}\cdot\eta_{b,n} \tag{16}$$

$$\eta_{b,n} = \frac{1}{\varepsilon^3\,\pi^{3/2}} \exp\left[-\left(\frac{\tau_{b,n}}{\varepsilon}\right)^2\right] \tag{17}$$

where n represents the actuator-line node index on blade b, N is the total number of nodes of each blade, B is the number of blades, $\tau_{b,n}$

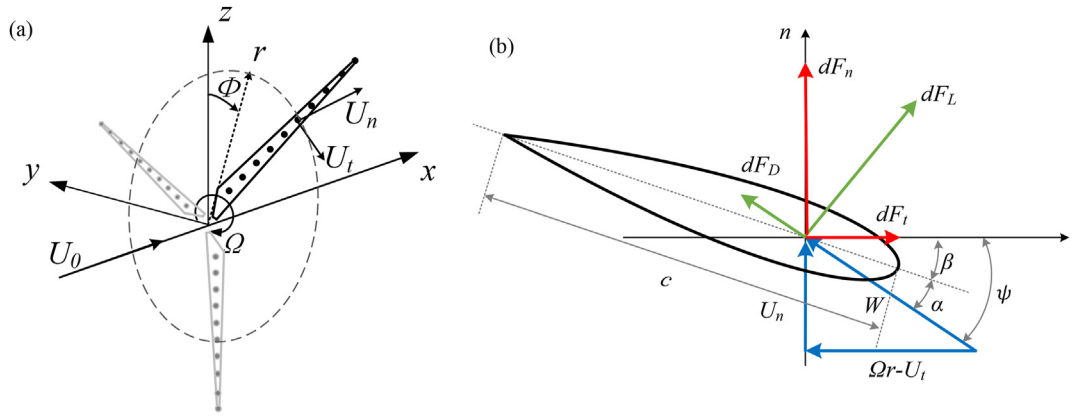

Fig. 1. Schematic of the ALM model for the turbine rotor: (a) actuator-line discretization of blades, (b) velocities and forces acting on a cross-sectional blade element.

denotes the distance from actuator-line node (b, n) to the computational cell center, and ε is a smoothing parameter to determine the force projection width. To maintain numerical stability [20], ε is taken equal to 2Δ, where Δ is grid size in rotor region. In the present wind turbine model, the nacelle and tower are modelled as porous media with 99.9% packing density [21].

It is worth mentioned that during the numerical simulation, the resulting aerodynamic torque Q_{aero} is computed by integration of the tangential forces along the blades, and the rotor speed Ω is determined from a drivetrain model expressed via the dynamic equation of rotor momentum balance as follows:

$$Q_{aero}\eta_M - N_{gear}Q_{gen} = \left(I_{rot} + N^2 I_{gen}\right)\frac{d\Omega}{dt} \tag{18}$$

where I_{rot} and I_{gen} denote the moments of the inertial of the rotor and generator, respectively, N_{gear} is the gearbox ratio, η_M is the gearbox efficiency, and Q_{gen} is the generator toque which are described in the following sections.

2.3. Wind turbine controller

A control logic proposed by Yamaguchi et al. [22] is used for the wind turbine controller. This controller is based on the one implemented by Jonkman et al. [23] with several improvements, in which, the wind turbine control is divided into three main control regions as shown in Fig. 2. In region 1, the wind turbine operates at minimum rotor speed Ω_{min}. When the rotor speed reaches Ω_0, the wind turbine operates as its maximum efficiency (region 2) and operates at a constant power in region 3. In region 1 and 2, the blade pitch angle is fixed to 0° and blade pitch control is activated in region 3. To smoothly connect the regions each other, region 1.5 and region 2.5 are defined. It is noted that regardless of the generator speed, if pitch angle is larger than θ_0, then the control region is region 3, as the pitch control needs to be activated. In this study, θ_0 is set to 1°.

2.3.1. Generator torque control

In this controller, the generator torque is given as a function of generator speed. In region 2, the control target is to achieve the maximum efficiency of the wind turbine. To achieve this, the generator torque Q_{R2} is controlled as a function of the rotor speed as shown in following equations.

$$Q_{R2} = k_{\text{opt}}{\Omega_f}^2 \tag{19}$$

$$k_{\text{opt}} = \frac{\pi\rho R^5 C_{p_{\text{opt}}}}{2N_{gear}^3 {\lambda_{\text{opt}}}^3 \eta_M} \tag{20}$$

where Ω_f is the low pass filtered rotor speed, ρ is the air density, R is the rotor diameter, $C_{p_{\text{opt}}}$ is the optimum power coefficient, λ_{opt} is the optimum tip speed ratio. The torque in region 3 is set to maintain the constant power as

$$Q_{R3} = \frac{P_r}{\Omega_f} \tag{21}$$

where P_r is the rated power.

Note that the demanded generator torques in region 2 and 3 are not continuous and, thus, require a transient zone between region 2 and 3 called region 2.5. In region 2.5, a steep change in the generator torque is needed, and this can be achieved by using the characteristic of induction generator as shown in the following equation.

$$Q_{R2.5} = k_s(\omega - \Omega_{\text{sync}}) \tag{22}$$

where, ω is the low pass filtered generator speed, Ω_{sync} is the synchronous speed of the induction generator and calculated by using

$$\Omega_{\text{sync}} = \frac{\Omega_r}{1 + 0.1S_g} \tag{23}$$

where, S_g is the slip of the induction generator and set to 5% in this study. The gradient k_s can be calculated by using

$$k_s = \frac{P_r/\Omega_r}{\Omega_r - \Omega_{\text{sync}}} \tag{24}$$

In this study, Ω_2 is set to Ω_r and Ω_1 is easily derived from Equations (19) and (22).

$$\Omega_1 = \frac{k_s - \sqrt{k_s(k_s - 4k_{\text{opt}}\Omega_{\text{sync}})}}{2k_{\text{opt}}} \tag{25}$$

To prevent the frequent switching between regions, fuzzy weight is used to smoothly connect the torque demand at the boundary of regions, i.e., the following equation is used to compute the generator torque demand Q for all the regions.

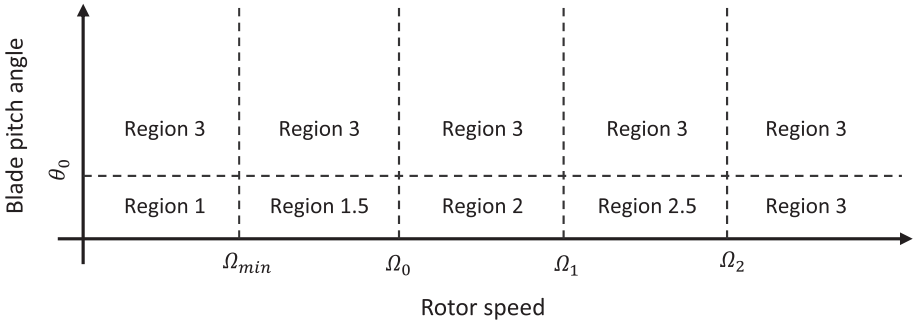

Fig. 2. Definition of wind turbine control regions.

$$Q = \frac{W_2 Q_{R2} + W_{2.5} Q_{R2.5} + W_3 Q_{R3}}{W_2 + W_{2.5} + W_3} \tag{26}$$

where Q_{R2}, $Q_{R2.5}$ and Q_{R3} are the torque demand for region 2, 2.5 and 3 respectively, as defined in equations (19), (21) and (22). W_2, $W_{2.5}$ and W_3 are the fuzzy weights based on both rotational speed and pitch angle as defined Yamaguchi et al. [22].

2.3.2. Blade pitch controller

The blade pitch angle demand is completely different in region 2 and region 3. In region 2, the pitch controller is not active, i.e., the pitch angle is set to zero as

$$\theta_{R2} = 0 \tag{27}$$

In region 2.5 and 3, the wind turbine operates at constant power by using pitch control. The blade pitch angle command θ_{PI} is given using PI control as shown in the following equation.

$$\theta_{R3} = \kappa(K_P e(t) + K_I u_I(t)) \tag{28}$$

where $K_p$is the proportional gain and K_I is the integral gain. These gain values are obatained based on the work done by Yoshida [24] as follows.

$$K_P = \frac{-T_{SI}\omega_c}{r\delta}\sqrt{\frac{\left(1 + T_A^2\omega_c^2\right)\left(\gamma^2 + J^2\omega_c^2\right)}{1 + T_{SI}^2\omega_c^2}} \tag{29}$$

$$K_I = \frac{K_P}{T_{SI}} \tag{30}$$

$$T_{SI} = \frac{\tan(\Phi_D - \Phi_M)}{\omega_c} \tag{31}$$

$$\gamma = \frac{\partial Q}{\partial \Omega} \tag{32}$$

$$\delta = \frac{\partial Q}{\partial \theta} \tag{33}$$

$$\Phi_M = \tan^{-1}\left(\frac{\gamma + JT_A\omega_c^2}{(\gamma T_A - J)\omega_c}\right) - \pi \tag{34}$$

where, J is the inertia moment around the rotor axis, T_A is the pitch actuator time constant, ω_c is the selectable gain cross frequency of speed control, Φ_M is the system phase margin, Φ_D is the design phase margin and T_{SI} is the integral time constant. In this study, T_A is set to 0.3, ω_c is set to 0.3 times the first modal angular frequency of the wind turbine tower and Φ_D is set to 50°. In addition, the following gain scheduling function is used for pitch control.

$$\kappa = \min\left(\frac{1}{(1-\xi) + \xi/\kappa_{out}}, 1\right) \tag{35}$$

$$\xi = \frac{\theta - \theta_{Des}}{\theta_{out} - \theta_{Des}} \tag{36}$$

$$\theta_{Des} = \theta_{min} + 0.05(\theta_{max} - \theta_{min}) \tag{37}$$

where θ is the measured pitch angle; θ_{Des} is the pitch angle design point; θ_{out} is the pitch angle at the cutout wind speed and is set to 90°; θ_{min} and θ_{max} are the minimum and maximum pitch angle and are set to 0° and 90°, respectively; and κ_{out} is the cut-out multiplicative gain and is set to 1/3.

In the controller by Jonkman et al. [23], the output of the integrator is saturated. This is to limit the output of the integrator, even in the case where the steady state output of the system is different from the reference speed. However, this may cause the controller to over speed. To solve this issue, Yamaguchi et al [22] proposed the use of and integral anti-windup K_{AW} technique of back calculation and tracking, as shown in Fig. 3. The pitch demand value from the PI controller θ_{PI} results in the rotor speed Ω under wind speed u. This dynamic is calculated through the aerodynamic simulation of the rotor and is written as $P(s)$.

2.3.3. Active yaw controller

Since the wind direction changes over time, a yaw system is required to keep the orientation of a wind turbine aligned with the wind direction to capture as much energy as possible. In this study, the yaw-rate control proposed by Fleming et al. [25] is adopted. Note that the yaw-rate control implementation does not provide continuous alignment, but intermittently aligns the turbine nacelle when a predefined threshold is exceeded. As schematically depicted in Fig. 4, the yaw error $e(t)$, i.e. the difference between the incoming wind direction $\vartheta(t)$ and the yaw position of the turbine $\gamma(t)$, is filtered by two low-pass filters, one with a cut-off frequency of $f_{fast} = 1/(2\pi T_{fast})$ Hz and the other $f_{slow} = 1/(2\pi T_{slow})$ Hz, producing a quickly and a slowly changing error. The quickly changing error $e_{fast}(t)$ is integrated and monitored. When the integrated error $E(t)$ reaches a threshold value E_{max}, the yaw position is moved with a constant yaw rate $\dot{\gamma}$ to the set point $\gamma_{set}(t)$ given by the slowly changing error. The value of yaw error threshold E_{max} is selected so that a continuous 10° of error will exceed the threshold after a certain accumulated period T_{acc}, i.e. $E_{max} = 100 T_{acc}\text{deg}^2\cdot s$. However, these control parameters for a utility-scale turbine is not

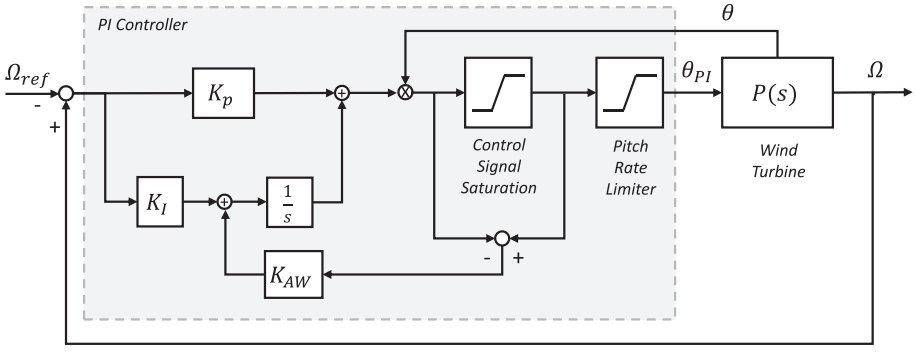

Fig. 3. The pitch controller implemented in the large eddy simulation.

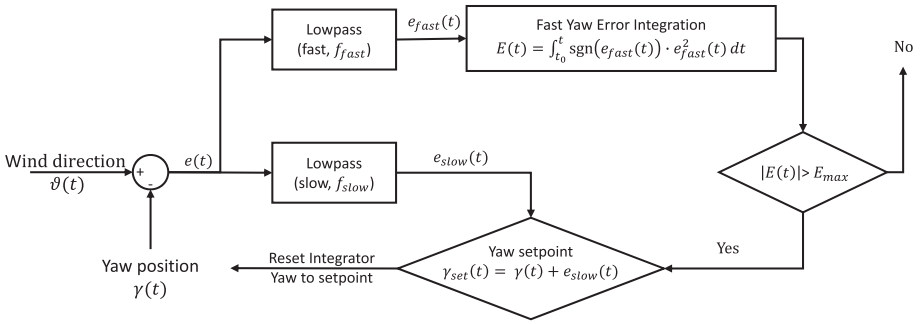

Fig. 4. The yaw controller implemented in the large eddy simulation.

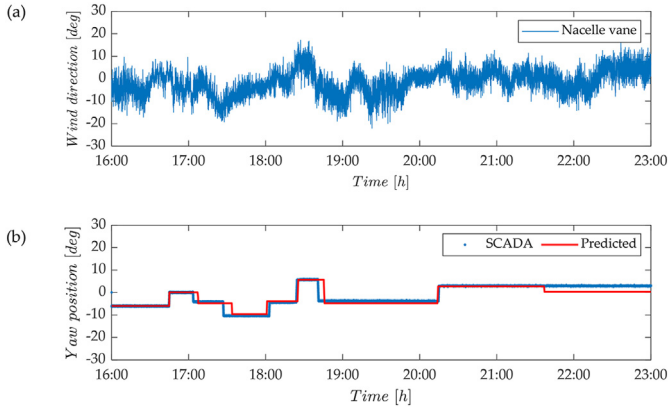

Fig. 5. Parameter identification for yaw control for a utility-scale 2.4 MW wind turbine at Choshi demonstration site: (a) time series of wind direction measured by Nacelle vane, and (b) comparison of yaw position between SCADA data and predicted values collected on September 28, 2016 from 16:00 to 23:00. The time series of wind direction and yaw position has subtracted the mean wind direction during the 7 h.

available due to the trade secret. Thus, the parameters used in current study are identified from the measurement data. The procedure of identification is briefly described as follows.

Firstly, the 1 Hz time-series of wind direction $\vartheta(t)$ measured by nacelle vane (see Fig. 5a) is input to the yaw control logic with guessed control parameters and the corresponding time-series of simulated yaw position $\gamma_{sim}(t)$ is calculated. For each simulation case, the root means square error (RMSE) of $\gamma_{sim}(t)$ with respect to the measured yaw position $\gamma_{mea}(t)$ is used to quantify the quality of estimation. The identification procedure can be subsequently treated as the optimization problem aims at finding a set of control

Table 1
Parameters used in yaw-rate control.

Parameter	Value
Fast Lowpass Filter Cutoff Frequency f_{fast}	1/17 Hz
Slow Lowpass Filter Cutoff Frequency f_{fast}	1/390 Hz
Yaw Rate $\dot{\gamma}$	0.3 deg/s
Yaw Error Threshold E_{max}	36000 deg^2·s

parameters $[T_{fast}, T_{low}, \dot{\gamma}, T_{acc}]^{opt}$ which minimize the RMSE of simulated time series of yaw position. The fmincon slover in MATLAB, a gradient-based optimization algorithm to find minimum of nonlinear problems with constraints, is adopted in this study to solve the defined optimization problem expressed in the following equation.

$$\begin{aligned} &\text{minimize} \quad RMSE\left(T_{fast}, T_{low}, \dot{\gamma}, T_{acc}\right) \\ &\text{subject to} \quad \begin{cases} 1/(2\pi) < T_{fast} < 20/(2\pi) & s \\ 60/(2\pi) < T_{slow} < 600/(2\pi) & s \\ \dot{\gamma} = 0.2 \text{ or } 0.3 & deg/s \\ 100 < T_{acc} < 600 & s \end{cases} \end{aligned} \tag{38}$$

The optimized control parameters based on the minimized RMSE are summarized in Table 1, the time-series of simulated yaw positions by using which are shown in Fig. 5b. Generally, the measured yaw positions can be well reproduced by using identified control parameters.

2.4. Wind turbine configuration

In this study, a laboratory-scale and a utility-scale wind turbine are introduced, as shown in Fig. 6. The laboratory-scale wind

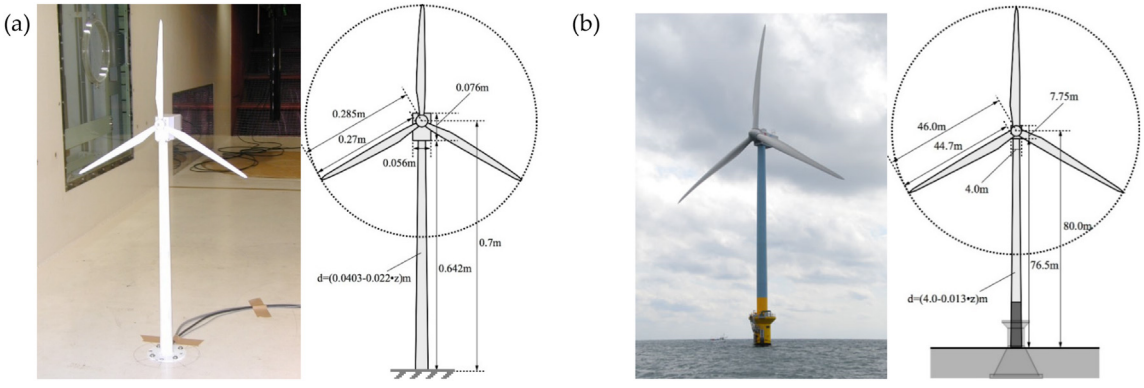

Fig. 6. Wind turbine and its dimensions: (a) laboratory-scale wind turbine in the wind tunnel test and (b) utility-scale wind turbine at Choshi demonstration site.

Table 2
Specification of the utility-scale wind turbine at Choshi demonstration site.

Parameters	Values
Rated capacity	2.4 MW
Hub height	80 m
Rotor diameter	92 m
Pitch control	Pitch to feather ($-2^\circ \sim 25.5^\circ$)
Rotor speed	Variable speed (9~15 rpm)
Cut-in wind speed	4 m/s
Cut-out wind speed	25 m/s

turbine is a 1/100 scale model of Mitsubishi's MWT-1000 used in the wind tunnel test by Ishihara et al. [26]; which has a rotor diameter of 0.57 m and a hub height of 0.7 m (See Fig. 6a). The detail of aerodynamic modelling for this model wind turbine including airfoil drag and lift coefficients and its validation can be found in Ref. [21]. The utility-scale one is the 2.4 MW wind turbine at Choshi offshore demonstration site as described in Refs. [27,28]. The specifications of the turbine are summarized in Table 2. As shown in Fig. 6b, it is an upwind turbine with a rotor diameter of 92 m and a hub height of 80 m. The aerodynamic modelling for Choshi 2.4 MW turbine and the control algorithm described in Section 2.3 have been validated by Yamaguchi et al. [22]. As shown in Fig. 7, power and thrust coefficients for different wind speed calculated by using the described model show good agreement with the bin average value of the measurements.

3. Verification of wind turbine control algorithm by FAST

Numerical setup of LES to investigate the wind turbine control is firstly described in Section 3.1. Two benchmarks with time-varying wind speed and time-varying wind direction are then performed in Section 3.2 and Section 3.3, respectively, where the wind turbine control algorithms for torque, pitch and yaw are verified.

3.1. Numerical setup

The utility-scale wind turbine model at Choshi offshore demonstration site is adopted to study the wind turbine control. As shown in Fig. 8, the computational domain has the streamwise length of 17D, the spanwise length of 6D and the height of 3.2D. The wind turbine model is placed at the center in the spanwise direction. The turbine rotor region ($x = -0.25D \sim 0.25D$ & $y = -0.75D \sim 0.75D$) is divided in a uniform distance of D/64 by structural mesh following the setting by Onel and Tuncer [29]. The time step size is set to $\Delta t = 0.01$s such that the tip of the rotor blades dose not travel through more than one mesh element per time step

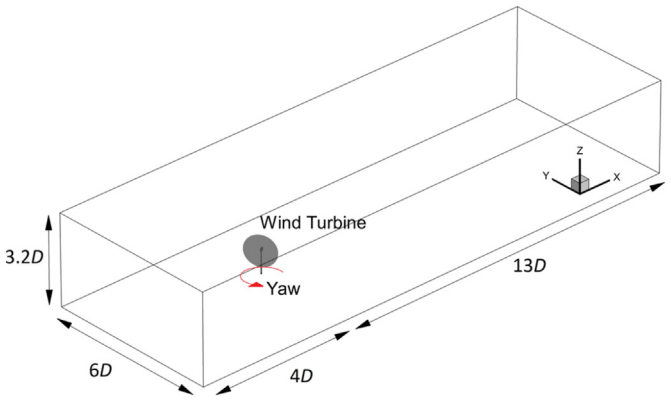

Fig. 8. Bird's eye view of the computational domain: wind turbine control simulation for a utility-scale Choshi-2.4 MW wind turbine under uniform inflow.

Table 3
Boundary conditions in simulations with benchmark wind conditions for wind turbine control

Boundary	Setting
Inlet	Uniform with predefined $u(t)$, $v(t)$
Outlet	Outflow
Side	Periodic
Top	Symmetric
Bottom	Symmetric

[30]. Boundary conditions used in the numerical simulations are summarized in Table 3. The inlet is set to a uniform velocity inflow, where the values of predefined time series of wind speed component of $u(t), v(t)$ are imposed for cases of time-varying wind speed and wind direction, respectively.

To validate the behavior of wind turbine controller implemented in LES code, step response simulations are performed by using two benchmark wind conditions, in which turbulence, wind shear, nacelle and tower shadow are not included.

The first benchmark [31] is a uniform inflow with time-varying wind speed and is used to test the behavior of the pitch and torque controller. As shown in Fig. 9a, this wind speed consists of two steps of above-rated wind speed (16 m/s and 14 m/s) and another two steps of under-rated wind sped (8.5 m/s and 10 m/s), where the rate of wind speed change between each step is 1 m/s^2.

Secondly, a 6-minitues time series of wind direction $\vartheta(t)$ is designed for the benchmark with time-varying wind direction. As shown in Fig. 10a, the time series include 3 steps starting from 0°,

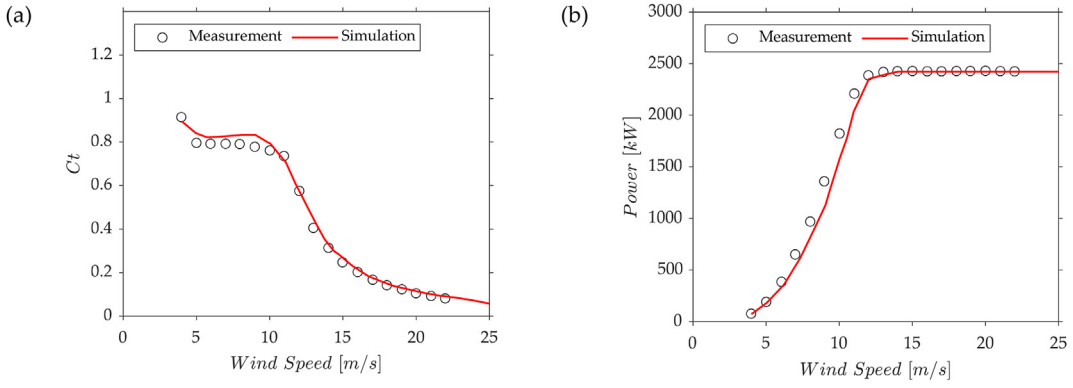

Fig. 7. Choshi 2.4 MW wind turbine operation curve: (a) thrust coefficient versus wind speed (b) power production versus wind speed.

falling to -30° and finally rising back to 0°. A fast transient and a slow transient with change rate of around 1.5 deg/s and 0.6 deg/s, respectively, are set and connected between steps through the cosine function following the Extreme coherent gust with direction change (ECD) model in IEC-61400-1 [32]. Note that the magnitude of wind speed vector in this benchmark keeps constant with a value of $U = 8$ m/s (region 2), and its components of $u = U\cos\theta(t)$ and $v = U\sin\theta(t)$ are imposed at the inlet of the computational domain (Fig. 8).

3.2. Benchmark with time-varying wind speed

The wind speed time series shown in Fig. 9a are inputted as the inlet condition of the computational domain, then the control signals of rotor speed, pitch angle are predicted and shown in Fig. 9b and c. At low wind speed of 8.5 m/s, the generator torque controller in region 2 is active and pitch angle is kept constant to zero. When wind speed steps to 10 m/s, a minus pitch angle of -2° is generated to make generator torque smoothed in region 2.5. At high wind speed of 16 m/s and 14 m/s, the pitch controller is activated, keeping the rotor speed constant to the rated value of 15 rpm. The step response of the pitch angle generator speed between each step does not present big overshoots and oscillations, which indicates that the gain scheduling in the controller is working properly. For comparison purpose, the simulation with same benchmark wind speed is also performed using FAST and the results are plotted by open circles in Fig. 9c~e. It is clearly seen that the steps in the wind speed yields changes in both thrust and torque force acting on the rotor, and the results predicted by the developed LES code agree well with those calculated by FAST.

3.3. Benchmark with time-varying wind direction

The step response of turbine operations and aerodynamic forces under time-varying wind direction are depicted in Fig. 10. The yaw position generally tracks the wind direction changes while presents a delay to it since the rate of wind direction change is much higher than that of yaw motor. Moreover, as the yaw control starts to operate only when the accumulated error exceeds the threshold, gaps between yaw angle and wind directions can be observed after the first and second transient, respectively. Due to these difference between wind direction and yaw angle, namely yaw misalignment, the wind speed normal to the rotor decreases, which yields to lower generator speed according to the optimum tip speed ratio in region 2. As a result, the response of thrust force and torque force vary up and down simultaneously following the change of rotor speed, since pitch angle is kept constant to zero. Remark also that the thrust and torque forces simulated by LES show favorable agreement with those calculated by FAST, which implies that the performance of pitch, torque and yaw controller implemented in the current LES code is verified.

4. Prediction of wake flows and dynamic loading of a laboratory-scale wind turbine

Numerical setup for a laboratory-scale wind turbine is described in Section 4.1. The wake flow is then predicted and validated with

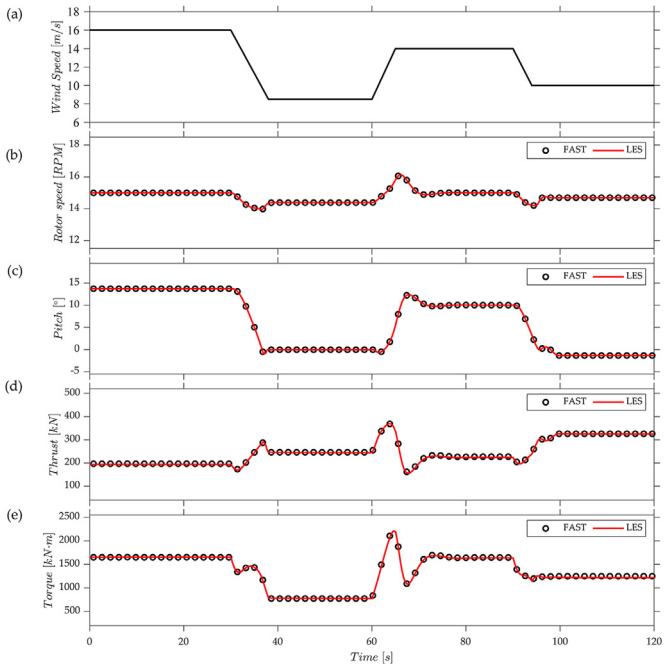

Fig. 9. Time series of (a) benchmark inflow wind speed, control signal of (b) rotor speed and (c) pitch angle, (d) rotor thrust force, and (e) rotor torque force.

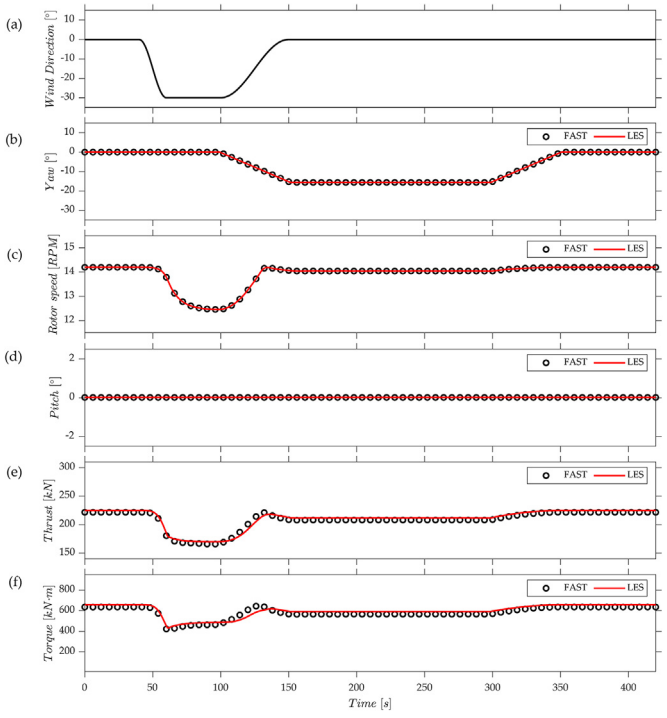

Fig. 10. Time series of (a) benchmark inflow wind direction, (b) control signal of yaw angle, (c) rotor speed, (d) pitch angle, (e) rotor thrust force, (f) rotor torque force.

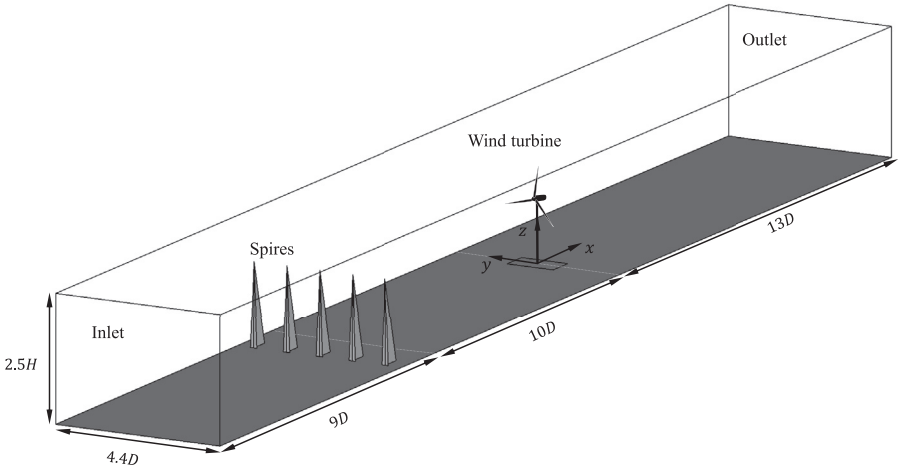

Fig. 11. Bird's eye view of the computational domain: wind turbine wake simulation for the laboratory-scale wind turbine in the wind tunnel test.

Table 4
Boundary conditions in simulations of laboratory-scale wind turbine.

Boundary	Setting
Inlet	Uniform with predefined $u(t)$, $v(t)$
Outlet	Outflow
Side	Periodic
Top	Symmetric
Bottom	Logarithm law

those obtained from the wind tunnel test in Section 4.2.

4.1. Numerical setup

As shown in Fig. 11, the computational domain has a streamwise length of 22D, a spanwise length of 4.4D and a vertical height of 3.2D, where D is the rotor diameter. The wind turbine model is placed at a distance of 10D from the spires and at the center in the spanwise direction. Boundary conditions used in the numerical simulations are summarized in Table 4. The velocity-inlet boundary condition is used with a uniform velocity and the outlet is set as outflow. Symmetry boundary condition is imposed at the top boundary and the side boundaries are set to be periodic. The wall-stress boundary condition is used at the ground surface and the surface of spires and fence based on the logarithmic law. The turbine rotor regions ($x = -0.25D \sim 0.25D$ & $y = -0.75D \sim 0.75D$) are divided in a uniform distance of D/64 by structural mesh following the setting by Onel and Tuncer. [29]. The time step size is selected such that the tip of the rotor blades dose not travel through more than one mesh element per time step [30]. The simulations for two kinds of operating condition ($C_T = 0.37$ and $C_T = 0.81$) under the inflow with the ambient turbulence intensity of $I_a = 0.035$ are conducted, where the tip speed ratio is set the same as the wind tunnel test.

4.2. Validation of predicted wake flow by wind tunnel measurement

Firstly, the atmosphere boundary layer without wind turbine is generated by the spires following the wind tunnel test. As shown in Fig. 12, the vertical mean speed and turbulence intensity profiles at the location of the turbine ($x = 0, y = 0$) show good agreement with the experiment data. Further, the mean velocity and turbulence intensity in the wake region for the 1/100 scaled turbine in wind tunnel test are shown in Fig. 13 and Fig. 14, respectively. The two-dimensional contours obtained from ALM simulation are displayed in the vertical x-z plane through the center of the turbine ($y = 0$). The numerical predicted vertical and horizontal profiles at selected downwind locations of $x = 2D$, $4D$, $6D$ and $8D$ are also plotted to illustrate the quantitative comparison between simulation results and the experimental data. Black dash lines and solid lines denote the results predicted by ADM-R and ALM, respectively. The experimental data are shown by open circles at two positions of x = 2D, 8D. All velocities are normalized by the freestream mean velocity U_{h0} at hub height, and the turbulence intensity is defined as the streamwise Reynolds stress σ_u normalized by U_{h0}. The x-axis denotes the distance from the wind turbine normalized by the rotor diameter D. The distance of $2D$ corresponds to a unit scale of normalized mean velocity U/U_{h0} in Fig. 13a and b and a scale of turbulence intensity with the value of 0.3 in Fig. 14a and b. The contours of mean velocity are characterized by a large velocity deficit in the near wake region, which extends gradually beyond 8D. And the contours of turbulence intensity reveal that an obvious enhancement of turbulence intensity is generated in the wake region, especially in the top tip level. From the comparison between the two cases, it can be observed that larger thrust coefficient induces stronger velocity deficit and turbulence intensity enhancement as well. In general, a good agreement is achieved between the numerical and experimental results of mean velocity and turbulence intensity, indicating that both LES with ADM-R and ALM can provide good accuracy in prediction of time averaged features of

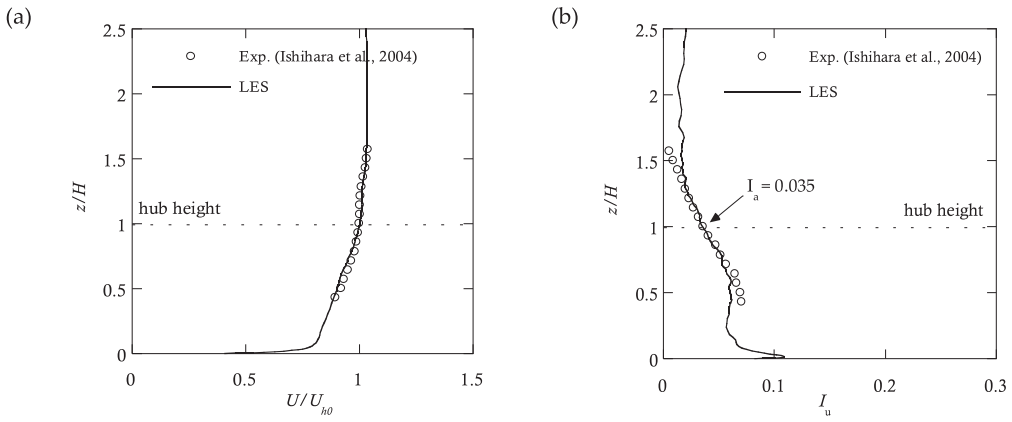

Fig. 12. Vertical profiles in the turbulence boundary layer without turbine in wind tunnel test: (a) Mean velocity and (b) Turbulence intensity.

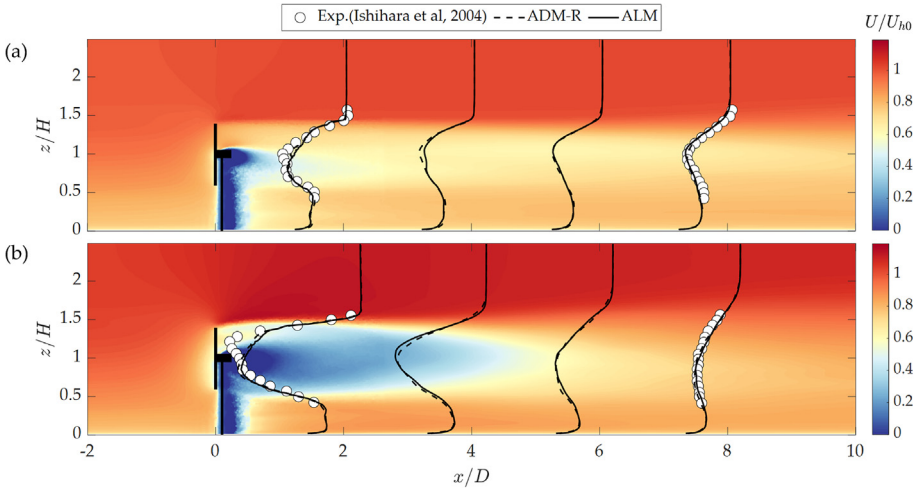

Fig. 13. Contours and profiles of mean velocity in the vertical x-z plane through the center of the rotor of laboratory-scale wind turbine: (a) Ct = 0.37, (b) Ct = 0.81.

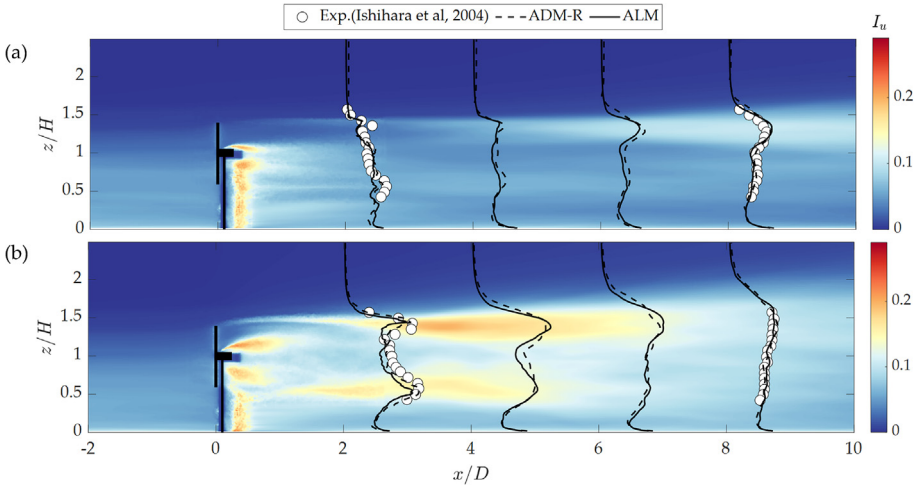

Fig. 14. Contours and profiles of turbulence intensity the vertical x-z plane through the center of the rotor of laboratory-scale wind turbine in the wind tunnel test: (a) Ct = 0.37, (b) Ct = 0.81.

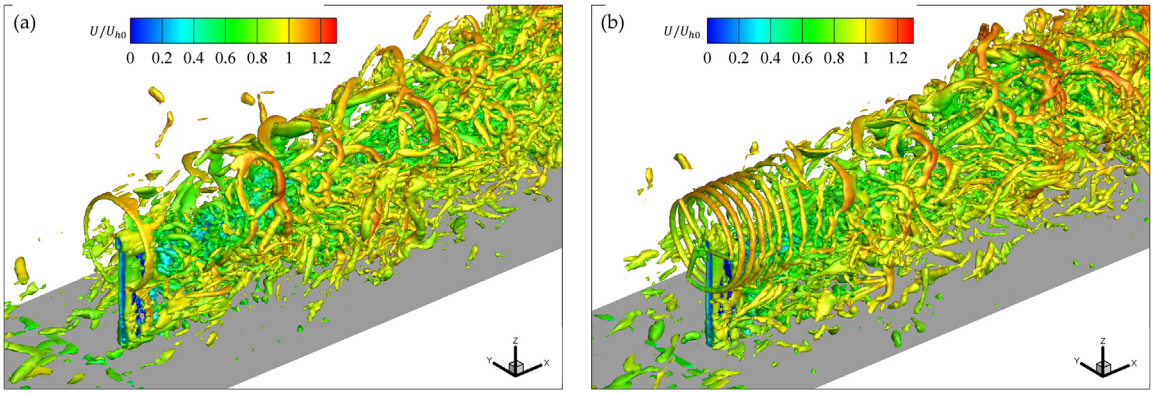

Fig. 15. Vortex structure in the wake flow of wind turbine: (a) ADM-R, (b) ALM.

wake flow, which is consistent with conclusions presented in other references [33,34].

The instantaneous three-dimensional behaviors of the flow field around and downstream the rotor for the case with Ct = 0.81 are depicted in Fig. 15, in which the vortex structures are visualized in terms of iso-surface plots of the Q-criterion [35] colored with normalized streamwise wind speed. The plot of ADM-R simulation clearly presents the ring-like vortex shedding from the edge of rotor disk in the near wake region. While for ALM, since the rotating blades is well modelled, the visualization gives a good impression of the helical structures of the distinct tip vortices within a distance of about 1D downstream the rotor. Due to the ambient turbulence mixing effect, the development of vortex in the far wake region simulated by ADM-R and ALM display almost similar features, where those rotor-induced coherent vortices break down into small-scale turbulence after a few rotor diameters. Further, Fig. 16 shows the normalized power spectrum of streamwise velocity sampled at different location downwind the turbine. For ALM simulation, a clear peak, induced by the blade rotation, appears at the tip side (y = 0.25D~0.75D) within very near wake region and dissipated after x = 0.5D. Though the three times the frequency of rotor rotation (3P frequency) in the near wake region could not be reproduced by ADM-R, the power spectrum in the downstream where $x \geq$1D shows almost the same distribution with those by ALM. It implies that, there would no direct contribution from upstream turbine wake to the dynamic response of downstream turbine.

To further clarify the blade rotation induced dynamic effect, a spectrum analysis for the time series of the thrust force sampled in the case with Ct = 0.81 is carried out for both ADM-R and ALM, and the result are depicted in Fig. 17. For comparison, an aerodynamic simulation for this case is also conducted by using FAST, in which the LES generated turbulent velocities on the rotor plane are sampled and used as the inflow for FAST simulation. Note that, the flexibility of blades and tower are not included in current simulations. In agreement with results calculated by FAST, a clear peak, coinciding with 3P frequency, appears in the power spectrum of thrust force calculated by ALM simulation, which however is not captured in the ADM-R. The 3P frequency are due to the fact that blades passing through ununiform flow fields which mainly comes from two effects known as wind shear and tower shadow [36]. These two effects would result in periodic fluctuations in both power output and dynamic loading. The above analysis is to emphasis that although ADM-R and ALM have almost same performance in prediction of time averaged features of wake flow, only ALM is capable of accurately evaluating the fatigue loads for a wind turbine with considering the blade rotation induced dynamic effects. On the other hand, for a wind farm simulation with target of power production only, ADM-R is competent enough.

5. Prediction of controls and wake flows of a utility-scale 2.4 MW wind turbine

The field measurements at the demonstration site and the numerical setup are described in Section 5.1. The predicted turbine control signals and wake flows are validated by the SCADA data and the Doppler scanning Lidar measurement in Section 5.2 and Section 5.3, respectively.

5.1. Desctiption of field measurements and numerical setup

To assess the accuracy of the developed control-oriented LES to simulate wind turbine operations and wakes in real scale, a field validation is conducted. The measurements are collected from the Choshi offshore wind energy test facility located about 3.5 Km offshore of Choshi city of Chiba prefecture, Japan. The detailed configuration of wind turbine has been introduced in Section 2.4. As shown in Fig. 18, a meteorological tower located 285 m east from the turbine. The meteorological tower has a height of 95 m, with cup anemometers and wind vanes installed between heights 20 m and 90 m at an interval of 10 m. The tower has a platform at a height of 15 m above the mean sea level. A Doppler scanning LiDAR (WindCube100S) is mounted on this platform. Note that measurements from the LiDAR were already validated against measurements from met mast tower [37,38].

The wind condition and turbine operation conditions collected on September 28, 2016 from 16:00 to 23:00 are selected to conduct the filed validation for current developed numerical code. Since the nacelle anemometer measured wind speed is influenced by the rotor and nacelle, the wind speed measured by the cup anemometers installed at a height of 80 m on the met mast tower is taken as the inflow condition. Fig. 19 shows the time series of the wind

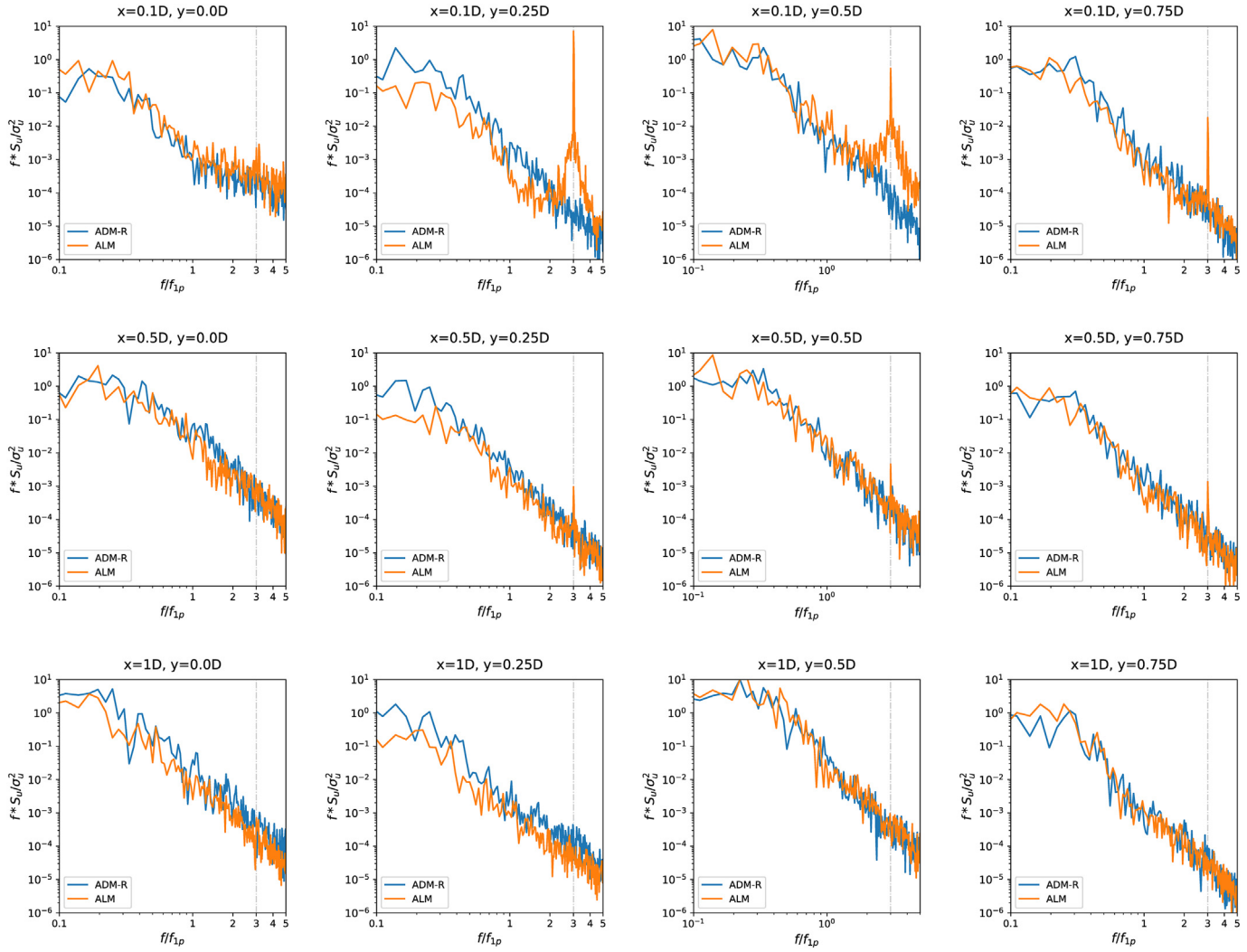

Fig. 16. Comparison of power spectrum of wind speed in the wake region obtained from the simulation of ADM-R and ALM. f denotes the ordinary frequency in Hz, and f_{1p} represents the frequency of rotor rotation.

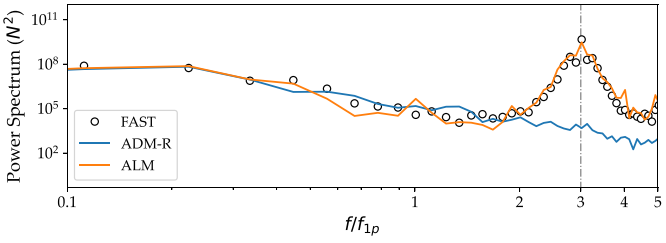

Fig. 17. Comparison of power spectrum of thrust forces obtained from the simulation of ADM-R, ALM, and FAST. f denotes the ordinary frequency in Hz, and f_{1p} represents the frequency of rotor rotation.

speed and wind direction sampled at 1 Hz during the 7 h period, where, in addition to the small scale (high frequency) fluctuations, a strong large scale (low frequency) time-variation are also observed. To reproduce this realistic wind variations in LES, following the implementation in Refs. [13,39]; the low frequency wind speed and wind direction changes are included using a low-pass filtered field measurement data as input, while the high-frequency fluctuations are directly resolved by micro-scale LES. Specifically, as shown in Fig. 19, the temporally varying wind speed and wind direction sample at 1 Hz is filtered through a low-pass filter with cutoff frequency of $f_c = 8 \times 10^{-4}$ Hz, which is almost equivalent to 10-min moving averaging, resulting a low frequently varied wind speed $\tilde{U}(t)$ and wind direction $\tilde{\vartheta}(t)$. The corresponding smoothed streamwise velocity components $u(t) = \tilde{U}(t)cos\tilde{\vartheta}(t)$ and

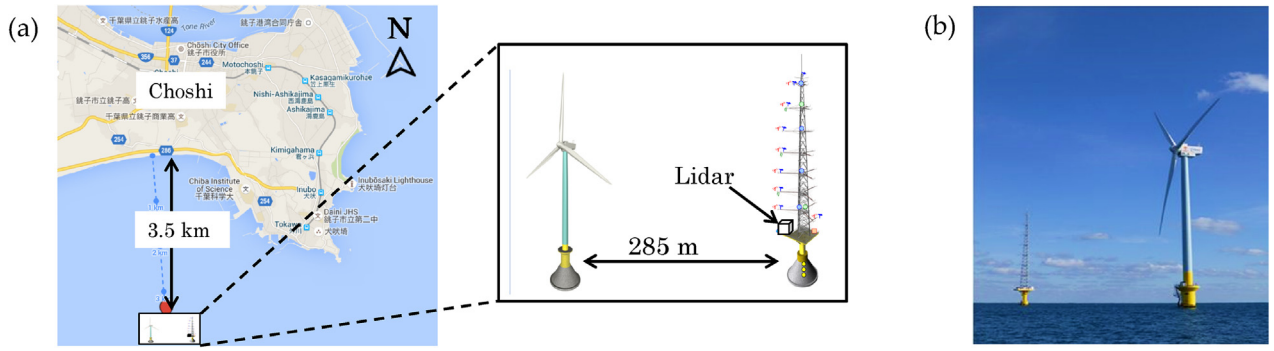

Fig. 18. Choshi offshore wind energy test facility. (a) lyaout and location shown in Google map, (b) picture of wind turbine and the met mast tower.

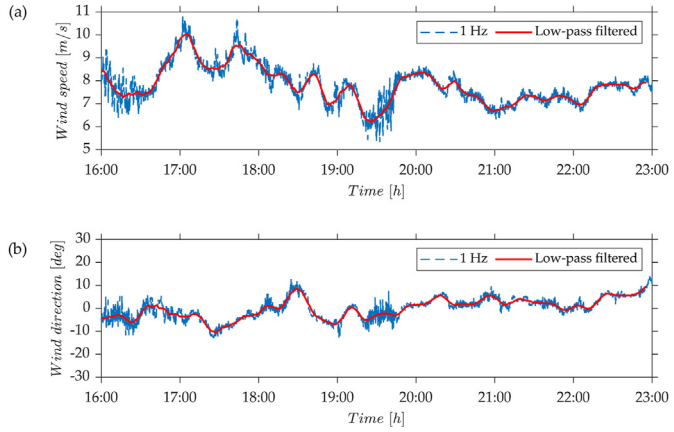

Fig. 19. Time series of (a) wind speed and (b) wind direction sampled at 1 Hz obtained from met mast at the height of 80 m. The low-pass filtered time series serve as input data to the LES. The time series of wind direction has subtracted the mean wind direction during the 7 h.

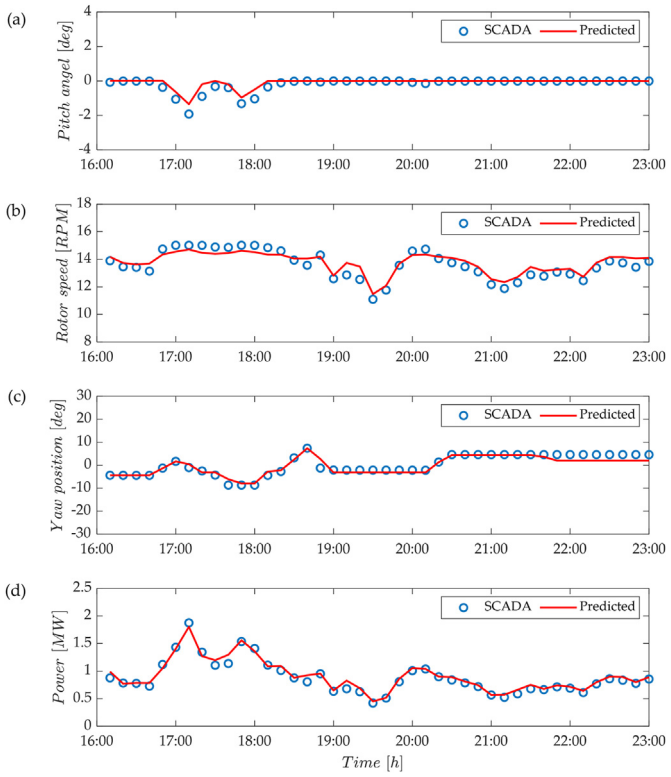

Fig. 20. Comparison of the time series of 10-minitue averaged (a) pitch angle, (b) rotor speed, (c) yaw position and (d) Power production between SCADA data and results predicted by LES. The time series of yaw position has subtracted the mean wind direction during the 7 h.

$v = \tilde{U}(t)\sin\tilde{\vartheta}(t)$ are then imposed to the inlet condition. In addition, the same spires in the wind tunnel (Section 4) is utilized to generate the ambient turbulence. As shown in Ref. [37], the average value of 10-min turbulence intensity during the validation period is around 3.5%, which is almost at the same level as the hub-height turbulence intensity generated by the spires (see Fig. 12). Therefore, it implies the turbulent inflow generated by spires can properly represent those high frequency fluctuations in the realistic time series. Note that, to run the simulation in real scale, the computational domain in Fig. 11 is upscaled by a ratio of $\lambda_L = 0.57/92$, while the original air viscosity is also amplified by λ_L to keep a same Reynolds number level as that in wind tunnel, so that the original mesh settings can be directly used without any further grid refinement. The boundary conditions are also identical to those mentioned in Table 4.

5.2. Validation of predicted turbine operation by SCADA data

In Section 5.2, the results of simulations focusing on the dynamic of the variables involved in the wind turbine controller are analyzed and compared against the field measurement. Fig. 20a, b, 20c and 20d show the temporal evolution of pitch angle, rotor speed, yaw position, and electric power, respectively, in which open circles represent predicted values and red solid lines denote those obtained from 10-min averaged turbine SCADA data. In general, good agreements are achieved in these results, which demonstrates that the utility-scale wind turbine operation conditions, including control signals and power production, are well reproduced by the developed numerical code. Looking at the time series, the wind speeds during the 7 h are below rated wind speed of 13 m/s,

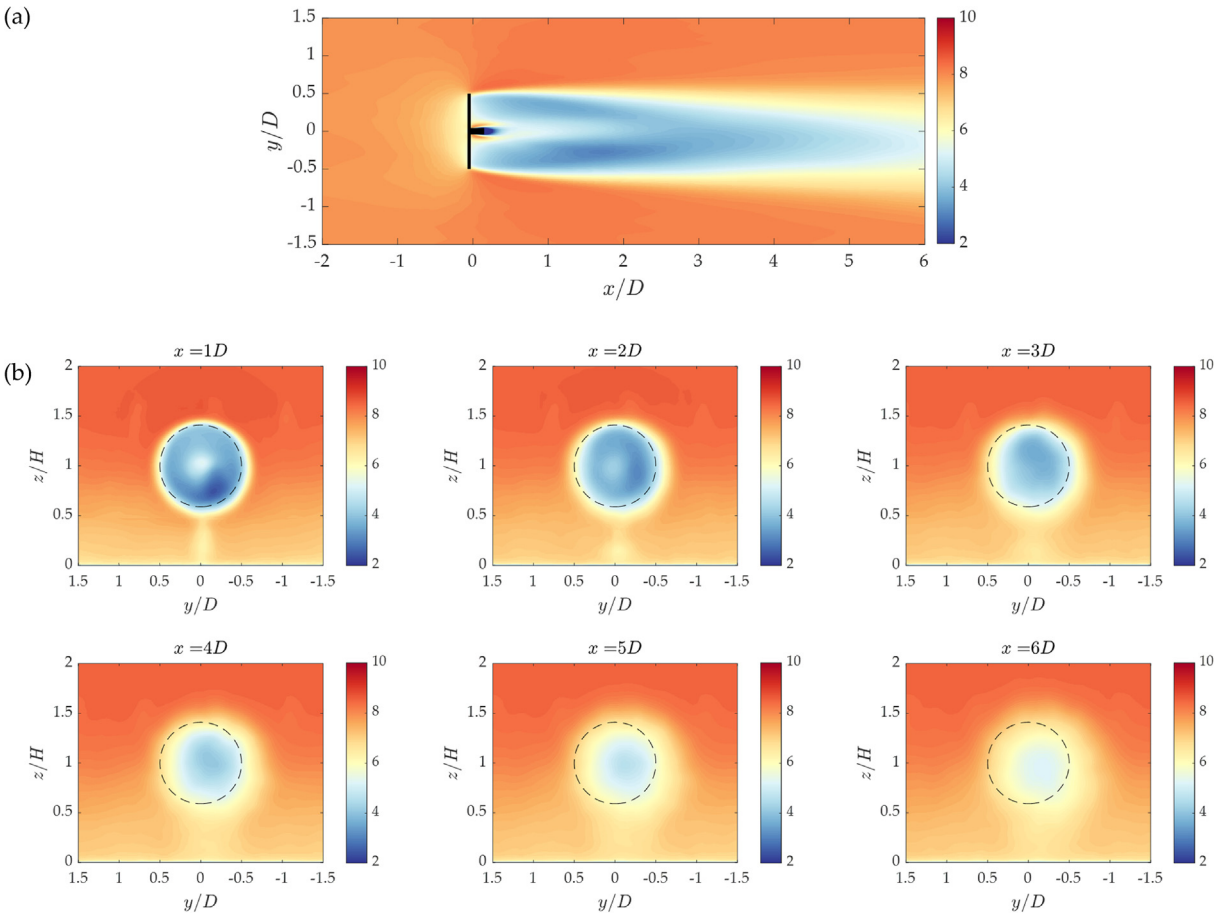

Fig. 21. Visualization of (a) mean wind speed at hub height and (b) mean wind speed at different downstream locations obtained from LES simulation of utility-scale wind turbine during validation period. The dashed lines in (b) denote the wind turbine rotor areas.

therefore, the pitch control is not working and take values of 0 in most of the time. As a result, the rotor speed and electric power generally follow the change of wind speed, except that during 16:45–18:15 where minus pitch angles are activated to smooth the rotor speed in region 2.5.

5.3. Validation of predicted wake flow by LiDAR measurement

In Section 5.3, the flow field around the turbine during the 7 h is simulated and then taken time averaged to characterize the wind turbine wake. Firstly, the simulation without time-varying wind direction is conducted to investigate the effect of Coriolis force on the wake deflection. Fig. 21a visualizes the mean velocity at the hub height, in which the x-axis and y-axis denote the distance from the rotor center normalized by the rotor diameter *D*. A dual peak velocity deficit is clearly visible in the near wake region and gradually get merged to one peak after x/D = 3. Furthermore, a slight wake deflection to the right-hand side can also be observed if seen from the front of turbine, which is induced by the Coriolis force effects. This deflection can be more clearly identified from the mean velocity contour on the vertical plane presented in Fig. 21b, where the z-axis denotes the height from the sea level normalized by the hub height *H*. The center of wake gradually deflects away from the rotor areas and its horizontal distance from rotor center reaches around 0.2D at the position of x/D = 6. Meanwhile, one can also see a considerable wake from nacelle and tower up to x/D = 1, which are also deflected which is due to the rotational flow field in the very near wake region.

In Fig. 22, the horizontal profiles of normalized velocity deficit at selected downwind locations are plotted to illustrate the quantitative comparison between simulation results and the measurement data obtained from PPI scans by scanning LiDAR [37]. To exclude the effects of time-varying wind direction, the LiDAR measured wind speed field at the hub height is transferred to a local wind coordinate, where x-axis is coincided with the 1-min-average wind direction at the midpoint of each scanning set. The transferred wind speeds are then taken time averaged for the whole 7 h. Note that, for $x \approx 2D$, the LiDAR scanning azimuth angles are approximately perpendicular to the incoming flow, where the measurement error is high and, therefore, the measured data is not

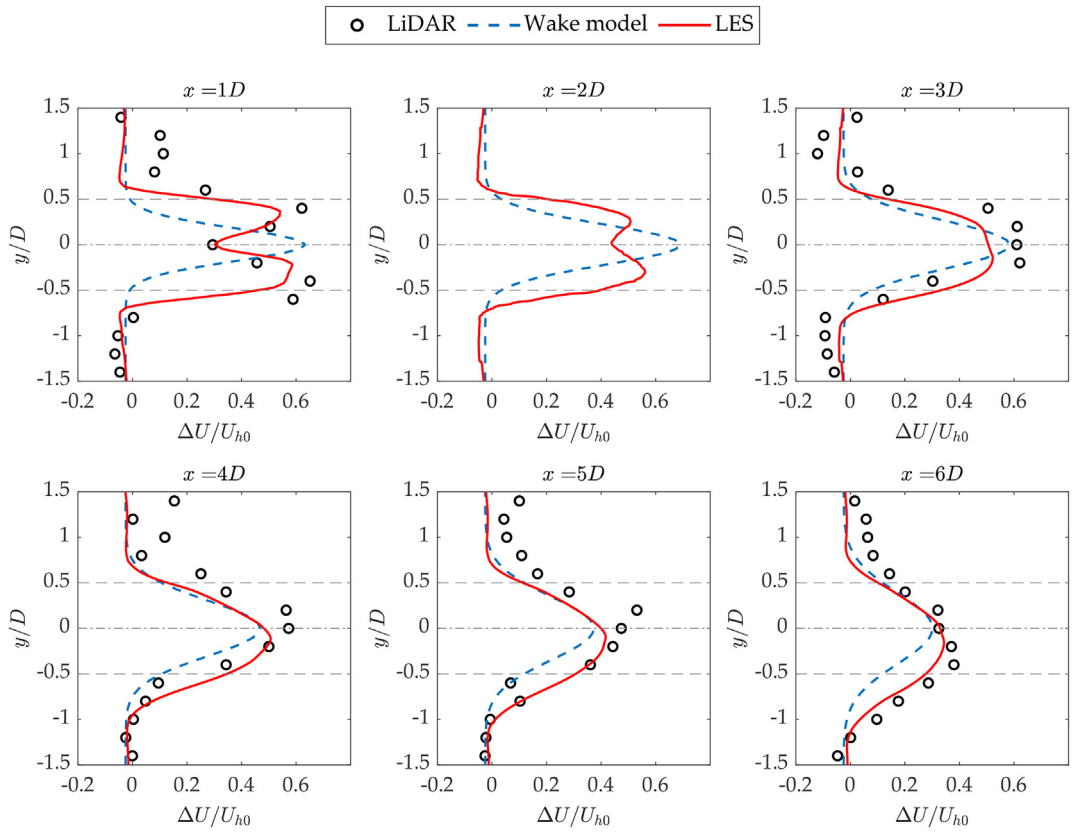

Fig. 22. Horizontal profiles of normalized velocity deficit at the hub height level and at various downstream locations of the wind turbine wake. The dot-dashed and dashed lines denote the wind turbine rotor center and rotor areas, respectively.

plotted in this region. Here, the normalized velocity deficit is defined as:

$$\frac{\Delta U}{U_{h0}} = \frac{U_{h0} - U}{U_{h0}} \tag{39}$$

where U_{h0} is the time averaged inflow velocity which is equal to 7.8 m/s during the current validation period, U is the streamwise velocity, and ΔU is the velocity deficit. The results predicted by a Gaussian-based wake model [40] are also plotted together for comparison. The calculation by wake model is performed in steady state, where a constant free stream wind speed of $U_{0,h}$, thrust coefficient value of 0.8 obtained from the $C_T - U$ curve (Fig. 5), and ambient turbulence intensity of 3.5% are used. The velocity deficit profiles predicted by LES show favorable agreement with the measured ones, which present a double-Gaussian distribution in the near wake up to x/D = 2, get flatted in the center zone at x/D = 3, and show a single-Gaussian distribution after x/D = 4. It is worth noting that, the Coriolis effects is of high importance to be considered in the wake steering control for utility-scale wind turbines, since it would have considerable influence on the wake deflections. However, the velocity profiles estimated by the conventional wake model present visible discrepancies from the measured values by LiDAR. Specifically, the double-Gaussian distribution in near the wake region could not be captured and the wake deflections from x = 4D to 6D are not reproduced since the Coriolis effects are ignored in the conventional wake model.

Finally, to clarify the effects of time-varying wind direction and yaw control, the wind speed field at the global coordinate are investigated, where x-axis is determined by a fixed direction coinciding with the mean wind direction during the 7 h. The same processing is conducted for LiDAR measured data. The mean velocity at the horizontal x-y plane of hub height, and vertical y-z plane of different locations are visualized in Fig. 23. By comparing the mean velocity distribution shown in Fig. 21, the following differences can be observed. First, the dual-peak in near wake region is getting faster to be converged to one peak up to $x = 2D$. Second, the velocity deficits show wider range and smaller values in the far wake region, especially at x = 5D and $x = 6D$. Third, the Coriolis force effects is less visible. These phenomena can be more clearly observed in Fig. 24, where time-averaged velocity deficit profiles extracted from LES and LiDAR data are compared and a favorable agreement is achieved. The evolution of velocity deficit profiles demonstrates that the wind direction change with dynamic yaw control will accelerate the wake expanding when the flow field is observed from a global fixed coordinate. It implies that the time-varying wind direction should be carefully considered in the power production estimation for a large-scale wind farm, which is

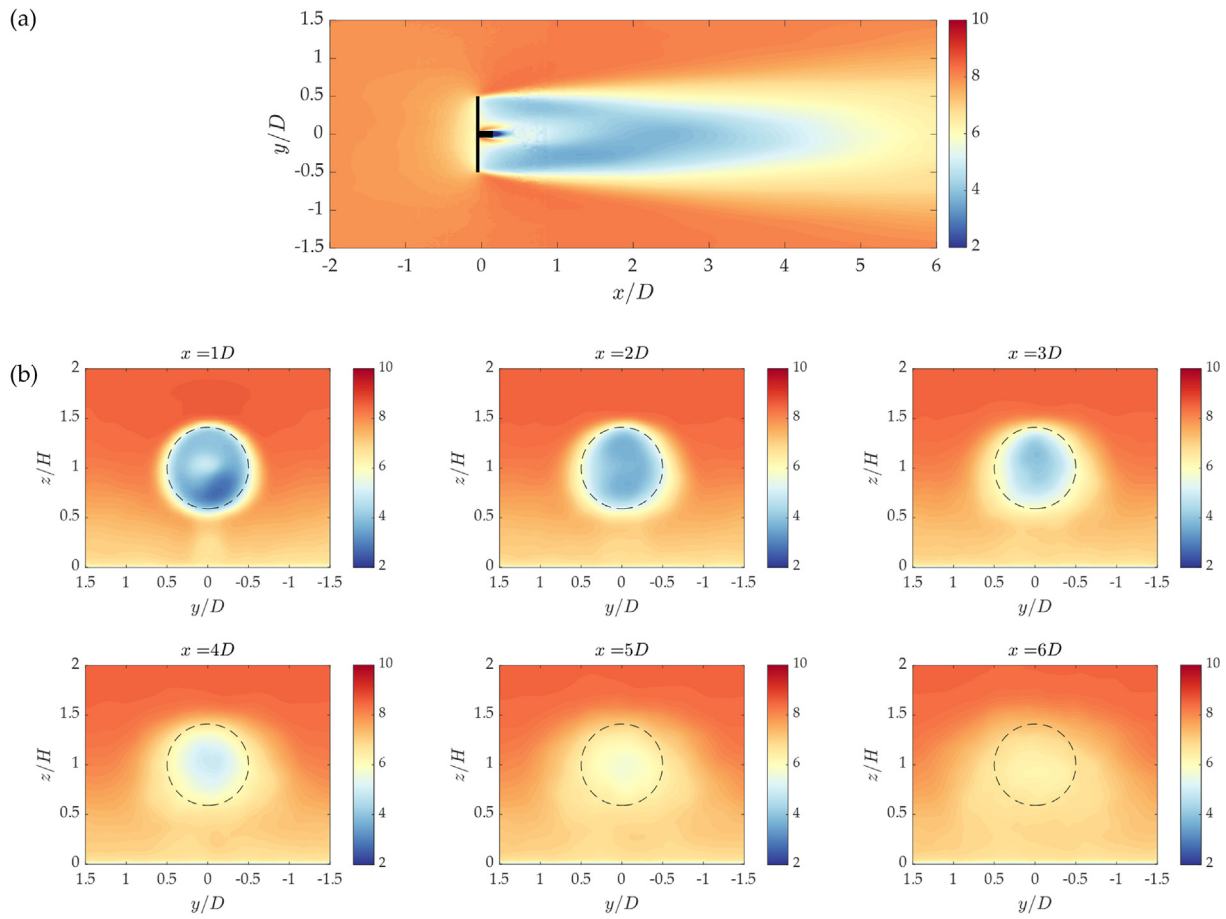

Fig. 23. Visualization of (a) mean wind speed at hub height and (b) mean wind speed at different downstream locations obtained from LES simulation of utility-scale wind turbine during validation period. The dashed lines in (b) denote the wind turbine rotor areas.

also clarified in Ref. [13]. For comparison, the velocity deficits calculated by the wake model are also plotted in Fig. 24. However, the wind speed calculated by the wake model fails to capture the wake expanding from x = 4*D* to 6*D* since the time varying wind direction and yaw misalignments are ignored in the steady state wake calculation.

6. Conclusions

In this study, the wind turbine torque, pitch, and yaw control algorithms are implemented in large eddy simulation, where the Actuator Line Model (ALM) is utilized to parameterize the rotational blades induced aerodynamics forces. The developed control-oriented LES code is then applied to predict the wake flows of laboratory-scale and utility-scale wind turbines. Following conclusions are obtained:

1. A control-oriented wind turbine simulation code is developed by implementing torque, pitch and yaw controls in large eddy simulation with ALM for the first time. Two sets of benchmark simulations with time-varying wind speeds and wind directions are performed, and the predicted thrust and torque forces agree well with those by FAST.
2. The predicted mean velocity and turbulence intensity in the wake of a laboratory-scale wind turbine show favorable agreement with those measured in wind tunnel experiments. It is observed based on the flow visualization and spectrum analysis that the blade rotation induced dynamic effects on the flow field in the far wake region can be negligible, however, their effects on dynamic loads on turbines are significant. ALM is capable of evaluating both power production and fluctuating load, while ADM-R is competent enough to serve for a wind farm simulation with target of predicting power production only.
3. Numerical simulations for a utility-scale wind turbine in an offshore demonstration site are conducted by using the developed control-oriented LES code. The time series of control signals and power production predicted by the developed controllers agree well with the SCADA data. The predicted mean velocity in the wind turbine wake with considering time-varying wind condition and Coriolis force show favorable agreement with the Doppler scanning LiDAR measurements.

Compared with existing approaches, the current developed

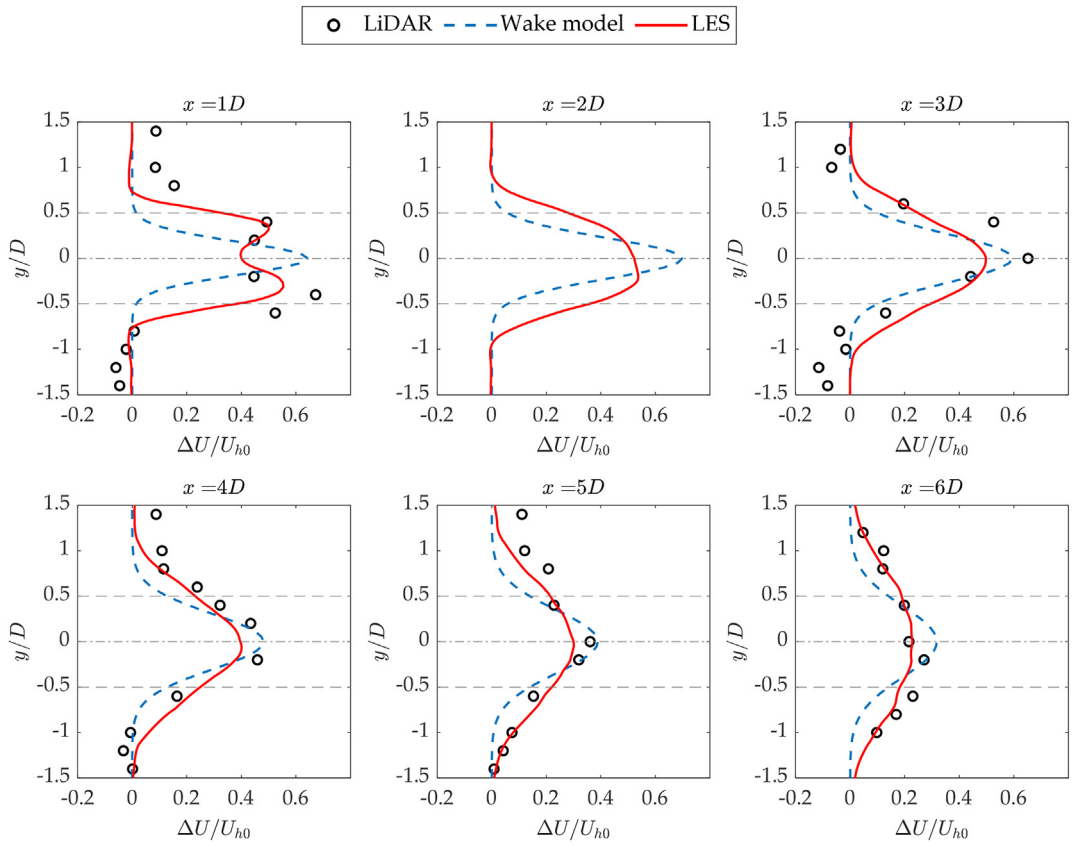

Fig. 24. Horizontal profiles of normalized velocity deficit at the hub height level and at various downstream locations of the wind turbine wake. The dot-dashed and dashed lines denote the wind turbine rotor center and rotor areas, respectively.

code incorporated an active yaw controller to address the time varying wind direction for the first time. However, the aero-elasticity considering a two-way coupling between the LES and a structural analysis model is not implemented yet and will be accomplished in the future work. Further validation focusing on the structural load on wind turbines will also be carried out.

Credit author statement

Takeshi Ishihara: Resources, Conceptualization, Methodology, Supervision, Writing-Reviewing and Editing. Guo-Wei Qian: Investigation, Software, Writing – original draft preparation, Formal analysis, Visualization. Yung-Peng Song: Data curation, Simulation.

Author contributions

This study was done by Yun-Peng Song, Guo-Wei Qian and Takeshi Ishihara. Guo-Wei Qian and Takeshi Ishihara designed the structure of the paper and wrote the paper.

Declaration of competing interest

The authors declare that they have no known competing financial interests or personal relationships that could have appeared to influence the work reported in this paper.

Acknowledgments

This research was carried out as a part of the project of social implementation of artificial intelligence technology for wind turbines funded by NEDO and supported by joint program for next generation of energy infrastructure with Toshiba Energy Systems & Solutions Corporation, J-POWER, Shimizu Corporation, MHI Vestas Offshore Wind Japan, ClassNK.. The authors express their deepest gratitude to the concerned parties for their assistance during this study.

References

[1] Kheirabadi AC, Nagamune R. A quantitative review of wind farm control with the objective of wind farm power maximization. J Wind Eng Ind Aerod 2019;192:45–73. https://doi.org/10.1016/j.jweia.2019.06.015.
[2] Van Wingerden JW, Fleming PA, Göcmen T, Eguinoa I, Doekemeijer BM, Dykes K, Lawson M, Simley E, King J, Astrain D, Iribas M, Bottasso CL, Meyers J, Raach S, Kölle K, Giebel G. Expert elicitation on wind farm control. J. Phys. Conf. Ser. 2020;1618. https://doi.org/10.1088/1742-6596/1618/2/022025.
[3] Breton SP, Sumner J, Sørensen JN, Hansen KS, Sarmast S, Ivanell S. A survey of modelling methods for high-fidelity wind farm simulations using large eddy simulation. Philos. Trans. R. Soc. A Math. Phys. Eng. Sci. 2017;375. https://doi.org/10.1098/rsta.2016.0097.
[4] Wu YT, Porté-Agel F. Modeling turbine wakes and power losses within a wind farm using LES: an application to the Horns Rev offshore wind farm. Renew Energy 2015;75:945–55. https://doi.org/10.1016/j.renene.2014.06.019.
[5] Sørensen JN, Shen WZ. Numerical modeling of wind turbine wakes. J Fluid Eng 2002;124:393–9. https://doi.org/10.1115/1.1471361.
[6] Deskos G, Laizet S, Palacios R. WInc3D: a novel framework for turbulence-resolving simulations of wind farm wake interactions. Wind Energy 2020;23:779–94. https://doi.org/10.1002/we.2458.
[7] Guggeri A, Draper M. Large eddy simulation of an onshore wind farm with the actuator line model including wind turbine's control below and above rated wind speed. Energies 2019;12:1–21. https://doi.org/10.3390/en12183508.
[8] Howland MF, González CM, Martínez JJP, Quesada JB, Larrañaga FP, Yadav NK, Chawla JS, Dabiri JO. Influence of atmospheric conditions on the power production of utility-scale wind turbines in yaw misalignment. J Renew Sustain Energy 2020;12. https://doi.org/10.1063/5.0023746.
[9] Liew J, Urbán A, Andersen SJ. Analytical model for the power-yaw sensitivity

of wind turbines operating in full wake. Wind Energy Sci. Discuss. 2019:1–18. https://doi.org/10.5194/wes-2019-65.
[10] Damiani R, Dana S, Annoni J, Fleming P, Roadman J, Van Dam J, Dykes K. Assessment of wind turbine component loads under yaw-offset conditions. Wind Energy Sci 2018;3:173–89. https://doi.org/10.5194/wes-3-173-2018.
[11] Simley E, Fleming P, Girard N, Alloin L, Godefroy E, Duc T. Results from a wake steering experiment at a commercial wind Plant : investigating the wind speed dependence of wake steering performance. Wind Energy Sci. Discuss. 2021;1–39. https://doi.org/10.5194/wes-2021-61.
[12] Munters W, Meneveau C, Meyers J. Turbulent inflow precursor method with time-varying direction for large-eddy simulations and applications to wind farms. Boundary-Layer Meteorol 2016;159:305–28. https://doi.org/10.1007/s10546-016-0127-z.
[13] Stieren A, Gadde SN, Stevens RJAM. Modeling dynamic wind direction changes in large eddy simulations of wind farms. Renew Energy 2021;170:1342–52. https://doi.org/10.1016/j.renene.2021.02.018.
[14] Van Der Laan MP, Sørensen NN. Why the Coriolis force turns a wind farm wake clockwise in the Northern Hemisphere. Wind Energy Sci 2017;2:285–94. https://doi.org/10.5194/wes-2-285-2017.
[15] Nouri R, Vasel-be-hagh A, Archer CL. The Coriolis force and the direction of rotation of the blades signi fi cantly a ff ect the wake of wind turbines 277. 2020. https://doi.org/10.1016/j.apenergy.2020.115511.
[16] Smagorinsky J. General circulation experiments with the primitive equations. Mon Weather Rev 1963;91:99–164. https://doi.org/10.1175/1520-0493(1963)091<0099:GCEWTP>2.3.CO;2.
[17] Bechmann A, Sørensen NN. Hybrid RANS/LES method for wind flow over complex terrain. Wind Energy 2010;13:36–50. https://doi.org/10.1002/we.346.
[18] Oka S, Ishihara T. Numerical study of aerodynamic characteristics of a square prism in a uniform flow. J Wind Eng Ind Aerod 2009;97:548–59. https://doi.org/10.1016/j.jweia.2009.08.006.
[19] Burton T, Sharpe D, Jenkins N, Bossanyi E. Wind energy handbook. second ed. Wiley; 2011.
[20] Martínez-Tossas LA, Churchfield MJ, Leonardi S. Large eddy simulations of the flow past wind turbines: actuator line and disk modeling. Wind Energy 2015;18:1047–60. https://doi.org/10.1002/we.1747.
[21] Ishihara T, Qian GW. A new Gaussian-based analytical wake model for wind turbines considering ambient turbulence intensities and thrust coefficient effects. J Wind Eng Ind Aerod 2018;177:275–92. https://doi.org/10.1016/j.jweia.2018.04.010.
[22] Yamaguchi A, Yousefi I, Ishihara T. Reduction in the fluctuating load on wind turbines by using a combined nacelle acceleration feedback and lidar-based feedforward control. Energies 2020;13:1–18. https://doi.org/10.3390/en13174558.
[23] Jonkman J, Butterfield S, Musial W, Scott G. Definition of a 5-MW reference wind turbine for offshore system development. Golden, CO (United States): National Renewable Energy Lab. (NREL); 2009. No. NREL/TP-500-38060.
[24] Yoshida S. Variable speed-variable pitch controllers for aero-servo-elastic simulations of wind turbine support structures. J Fluid Sci Technol 2011;6:300–12. https://doi.org/10.1299/jfst.6.300.
[25] Fleming PA, Scholbrock AK, Jehu A, Davoust S, Osler E, Wright AD, Clifton A. Field-test results using a nacelle-mounted lidar for improving wind turbine power capture by reducing yaw misalignment. J. Phys. Conf. Ser. 2014;524:012002. https://doi.org/10.1088/1742-6596/524/1/012002.
[26] Ishihara T, Yamaguchi A, Fujino Y. Development of a new wake model based on a wind tunnel experiment. Glob. Wind Power. 2004.
[27] Oh S, Ishihara T. Structural parameter identification of a 2.4 MW bottom fixed wind turbine by excitation test using active mass damper. Wind Energy 2018;21:1232–8. https://doi.org/10.1002/we.2214.
[28] Yamaguchi A, Sarli PW, Ishihara T. Extreme load estimation of the wind turbine tower during power production. Wind Eng 2019;45:93–106. https://doi.org/10.1177/0309524X19872766.
[29] Onel HC, Tuncer IH. Investigation of wind turbine wakes and wake recovery in a tandem configuration using actuator line model with LES. Comput Fluids 2021;220:104872. https://doi.org/10.1016/j.compfluid.2021.104872.
[30] Troldborg N. Actuator line modeling of wind turbine wakes. The Technical University of Denmark (DTU); 2009.
[31] Hand MM, Balas MJ. Systematic controller design methodology for variable-speed wind turbines. Wind Eng 2000;24:169–87. https://doi.org/10.1260/0309524001495549.
[32] IEC 61400-1. Wind turbines - Part 1: design requirements. 2019.
[33] Draper M, Guggeri A, Usera G. Validation of the Actuator Line Model with coarse resolution in atmospheric sheared and turbulent inflow. J. Phys. Conf. Ser. 2016;753. https://doi.org/10.1088/1742-6596/753/8/082007.
[34] Porté-Agel F, Wu Y-T, Lu H, Conzemius RJ. Large-eddy simulation of atmospheric boundary layer flow through wind turbines and wind farms. J Wind Eng Ind Aerod 2011;99:154–68. https://doi.org/10.1016/j.jweia.2011.01.011.
[35] Jeong J, Hussain F. On the identification of a vortex. J Fluid Mech 1995;285:69–94. https://doi.org/10.1017/S0022112095000462.
[36] Dolan DSL, Lehn PW. Simulation model of wind turbine 3p torque oscillations due to wind shear and tower shadow. IEEE PES Power Syst. Conf. Expo. PSCE 2006 - Proc. 2006;21:2050–7. https://doi.org/10.1109/PSCE.2006.296240. 2006.
[37] Goit JP, Yamaguchi A, Ishihara T. Measurement and prediction of wind fields at an offshore site by scanning Doppler LiDAR and WRF. Atmosphere 2020;11. https://doi.org/10.3390/ATMOS11050442.
[38] Kikuchi Y, Fukushima M, Ishihara T. Assessment of a coastal offshorewind climate by means of mesoscale model simulations considering high-resolution land use and sea surface temperature data sets. Atmosphere 2020;11:1–16. https://doi.org/10.3390/ATMOS11040379.
[39] Chatterjee T, Cherukuru NW, Peet Y, Calhoun R. Incorporating realistic geophysical effects of mean wind from LIDAR measurements in large eddy simulation of wind turbine arrays. 35th Wind Energy Symp 2017:1–17. https://doi.org/10.2514/6.2017-1165. 2017.
[40] Qian GW, Ishihara T. A new analytical wake model for yawed wind turbines. Energies 2018;11(3):665. https://doi.org/10.3390/en11030665.